We are IntechOpen,
the world's leading publisher of
Open Access books
Built by scientists, for scientists

6,900
Open access books available

186,000
International authors and editors

200M
Downloads

Our authors are among the

154
Countries delivered to

TOP 1%
most cited scientists

12.2%
Contributors from top 500 universities

BOOK
CITATION
INDEX
CLARIVATE ANALYTICS
INDEXED

WEB OF SCIENCE™

Selection of our books indexed in the Book Citation Index
in Web of Science™ Core Collection (BKCI)

Interested in publishing with us?
Contact book.department@intechopen.com

Sintering and Properties of Nb$_4$AlC$_3$ Ceramic

Chunfeng Hu[1], Qing Huang[1],
Yiwang Bao[2] and Yanchun Zhou[3]
[1]Ningbo Institute of Material Science and Technology,
Chinese Academy of Sciences, Ningbo
[2]State Key Laboratory of Green Building Materials,
China Building Materials Academy, Beijing
[3]Ceramic and Composites, Aerospace Research
Institute of Materials and Technology, Beijing,
China

1. Introduction

Layered ternary compounds, M$_{n+1}$AX$_n$ (where M is an early transition metal, A is an A group element, X is C or N, and n = 1-3), also called the MAX phases, are layered carbides or nitrides crystallizing with hexagonal symmetry structure [1,2]. These ceramics combine the characteristics of metals and ceramics such as high strength and modulus, low density, good electrical and thermal conductivity, easy machinability, damage tolerance, and resistance to thermal shock and high temperature oxidation. To date, more than 50 M$_2$AX compounds (not list for brevity), five M$_3$AX$_2$ compounds (Ti$_3$SiC$_2$, Ti$_3$GeC$_2$, Ti$_3$AlC$_2$, Ta$_3$AlC$_2$, and Ti$_3$SnC$_2$), and seven M$_4$AX$_3$ (Ta$_4$AlC$_3$, Ti$_4$AlN$_3$, Ti$_4$SiC$_3$, Ti$_4$GeC$_3$, Nb$_4$AlC$_3$, V$_4$AlC$_3$, and Ti$_4$GaC$_3$) were identified. For 413 phases, it has been determined that there are two kinds of atomic stacking sequences along [0001] direction. Ti$_4$AlN$_3$, Ti$_4$SiC$_3$, Ti$_4$GeC$_3$, α-Ta$_4$AlC$_3$, Nb$_4$AlC$_3$, and V$_4$AlC$_3$ have the same Ti$_4$AlN$_3$-type crystal structure with atomic arrangement of AB<u>A</u>BAC<u>B</u><u>C</u>BC along [0001] direction. Only β-Ta$_4$AlC$_3$ was determined to have the AB<u>A</u>BAB<u>A</u>BAB atomic arrangement along [0001] direction. In detail, the difference of atomic arrangements between β-Ta$_4$AlC$_3$ and α-Ta$_4$AlC$_3$ lay in the diversity of atomic positions. The atomic positions of β-Ta$_4$AlC$_3$ were described as Ta1 at (4f) (1/3, 2/3, 0.05524), Ta2 at (4f) (2/3, 1/3, 0.16016), Al at (2c) (1/3, 2/3, 1/4), C1 at (2a) (0, 0, 0), and C2 at (4e) (0, 0, 0.11125). While, the atomic positions of α-Ta$_4$AlC$_3$ were determined as Ta1 at (4f) (1/3, 2/3, 0.05453), Ta2 at (4e) (0, 0, 0.15808), Al at (2c) (1/3, 2/3, 1/4), C1 at (2a) (0, 0, 0), and C2 at (4f) (2/3, 1/3, 0.10324).

Ti$_4$AlN$_3$-type Nb$_4$AlC$_3$ was firstly discovered by heat treating Nb$_2$AlC at 1700°C, and the crystal structure was determined using a combined technique of *ab initio* calculation and high resolution scanning transmission electron microscopy. Additionally, the single phase Nb$_4$AlC$_3$ could be synthesized by hot pressing and spark plasma sintering. The microstructure, electrical, thermal, and mechanical properties of as-prepared Nb$_4$AlC$_3$ were systematically described.

2. Crystal structure

Figure 1 compares the projection of atoms (Figs. 1(a) and (b)) and the Z-contrast image of Nb_4AlC_3 (Fig. 1(c)), wherein the layer stacking sequence of Nb and Al atoms along the [0001] direction was directly shown. In one Nb-C slab, the number of Nb layers was four, i.e., the regular atomic arrangement was four Nb atoms layers per Al atoms layer alternately stacking along the [0001] direction. The Nb layers were separated by close packed Al atom (0001) planes. The Z-contrast image confirmed that the Nb_4AlC_3 crystallized in the Ti_4AlN_3-type crystal structure. It basically consisted of two units: nonstoichiometric $NbC_{0.75}$ slab and Al atomic plane. The atom arrangement of Nb and Al was AB$\underline{A}$BACB$\underline{C}$BC [3].
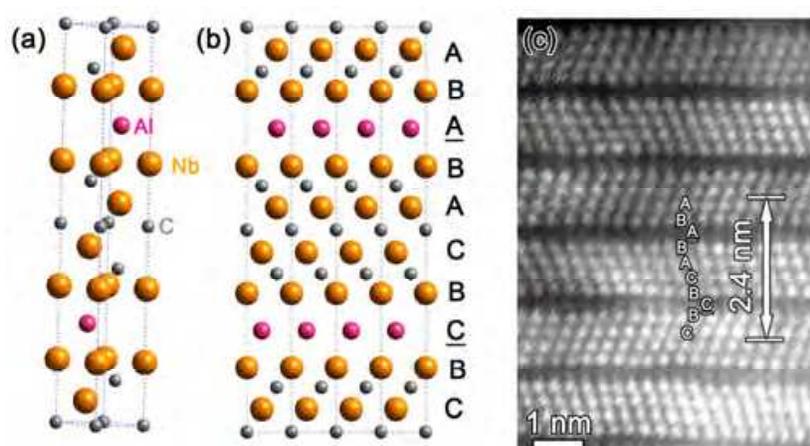

Fig. 1. (a) and (b) Atom arrangement of Nb_4AlC_3. (c) High-resolution Z-contrasting TEM image after FFT filtering of Nb_4AlC_3 [3].

3. Hot pressing

3.1 Synthesis procedure

Commercial powders of niobium (99%, -200 mesh), aluminum (99%, -300 mesh), and graphite (99%, -200 mesh) were used as starting materials. Firstly, the molar ratio of Nb : Al : C = 4 : 1.3 : 2.7 was selected for investigating the reaction path of Nb_4AlC_3. Excess Al and less graphite were used because Al might lose during high temperature processing and C-deficient existed in most of Al-containing MAX phases. The powders were dryly mixed in a resin jar, ball milled for 12 hours, and then sieved. The mixed powders were uniaxially pressed at 5 MPa to form the green compacts in a BN-coated graphite die. Afterwards, the green compacts were heated to 1500, 1550, 1600, 1650, and 1700°C, with a heating rate of 15°C/min in a flowing Ar atmosphere. The samples were held at target temperatures for 60 minutes under a pressure of 5 MPa, and then cooled down to room temperature with the furnace cooling rate. After composition optimization, single-phase dense Nb_4AlC_3 was

prepared using the starting materials with the molar ratio of Nb : Al : C = 4 : 1.1 : 2.7. The green compact was held at 1700°C for 60 minutes under a pressure of 30 MPa.

Temperature	Phase compositions
1500°C	NbC, Nb$_2$AlC, Nb$_4$AlC$_3$, C, Nb$_2$Al, Al$_3$Nb, Nb$_3$Al$_2$C
1550°C	NbC, Nb$_2$AlC, Nb$_4$AlC$_3$, Al$_3$Nb
1600°C	NbC, Nb$_2$AlC, Nb$_4$AlC$_3$, Al$_3$Nb
1650°C	Nb$_2$AlC, Nb$_4$AlC$_3$, Al$_3$Nb
1700°C	Nb$_4$AlC$_3$, Al$_3$Nb

Table 1. Phase compositions of the samples sintered at the temperatures range from 1500 to 1700°C [4].

Figure 2 shows the X-ray diffraction patterns of the samples sintered at 1500-1700°C using initial powders with the molar ratio of Nb : Al : C = 4 : 1.3 : 2.7. The identified phase compositions of the samples were listed in Table 1. At 1500°C, the phases in the sample were NbC, Nb$_2$AlC, Nb$_4$AlC$_3$, C, Nb$_2$Al, Al$_3$Nb, and Nb$_3$Al$_2$C (Fig. 2(a)). As the temperature was raised to 1550°C, only NbC, Nb$_2$AlC, Nb$_4$AlC$_3$, and Al$_3$Nb were detected in the sample (Fig. 2(b)). C, Nb$_2$Al, and Nb$_3$Al$_2$C were completely consumed. The formation of Nb$_2$AlC was probably associated with the reactions in equations (1) and (2):

$$Nb_2Al + C = Nb_2AlC \tag{1}$$

$$Nb_3Al_2C + NbC = 2Nb_2AlC \tag{2}$$

When the temperature increased to 1600°C, the amount of Nb$_4$AlC$_3$ increased with the consumption of Nb$_2$AlC and NbC (Fig. 2(c)). Possibly, the reaction occurred as following:

$$Nb_2AlC + 2NbC = Nb_4AlC_3 \tag{3}$$

When the temperature reached 1650°C, the diffraction peaks of NbC disappeared. The main crystalline phase was Nb$_4$AlC$_3$, together with small quantities of Nb$_2$AlC and Al$_3$Nb (Fig. 2(d)). When a higher temperature of 1700°C was used, the final sample contained only Nb$_4$AlC$_3$ and Al$_3$Nb (Fig. 2(e)). All diffraction peaks of Nb$_2$AlC disappeared. The decomposition reaction could be described as:

$$9Nb_2AlC = 3Nb_4AlC_3 + 2Al_3Nb + 4Nb \tag{4}$$
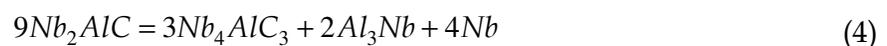
Figure 3 shows the X-ray diffraction pattern of single phase Nb$_4$AlC$_3$. All the diffraction peaks corresponded to Nb$_4$AlC$_3$. The crystal structure of Nb$_4$AlC$_3$ prepared by the present method was Ti$_4$AlN$_3$-type. No impurity phases were detected.
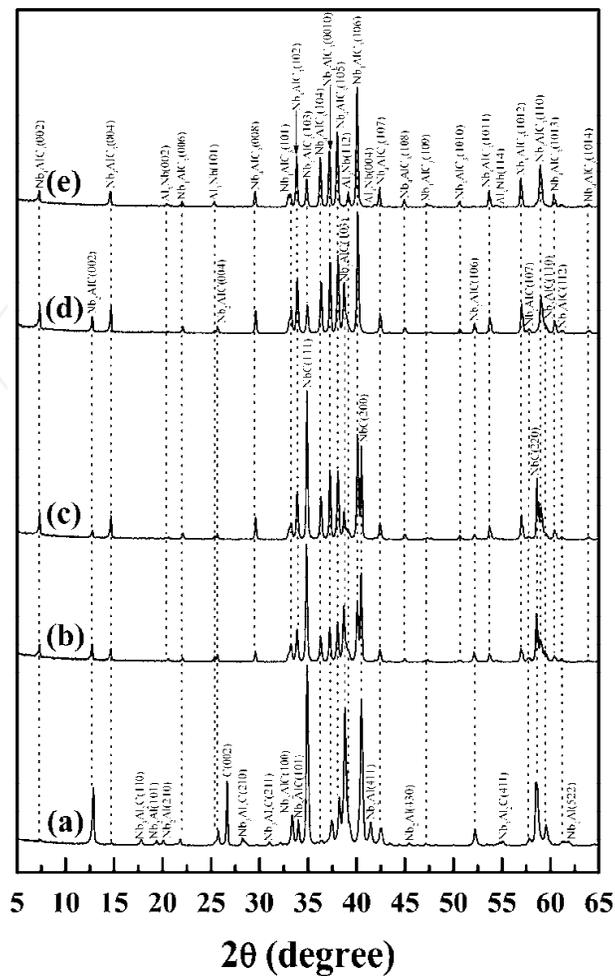
Fig. 2. X-ray diffraction (XRD) patterns of initial powders with the molar ratio of Nb : Al : C = 4 : 1.3 : 2.7 sintered at (a) 1500°C, (b) 1550°C, (c) 1600°C, (d) 1650°C, and (e) 1700°C [4].
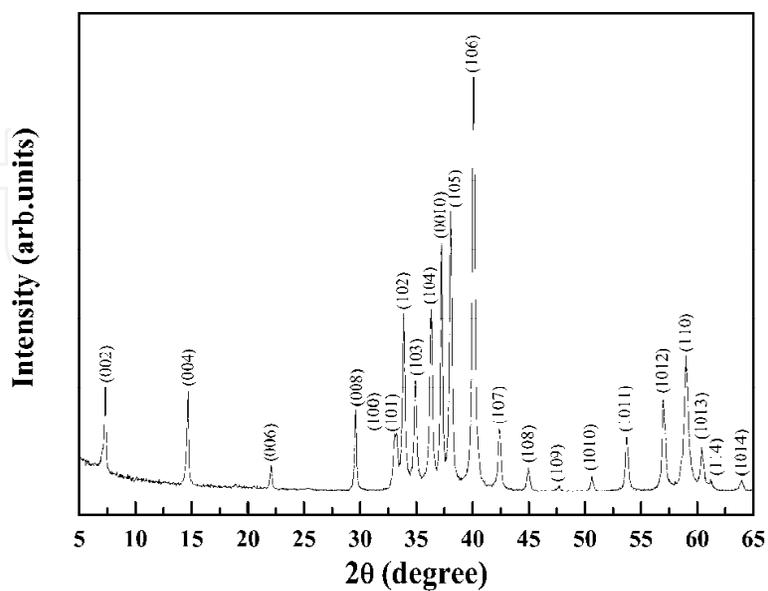
Fig. 3. XRD pattern of Nb$_4$AlC$_3$ prepared using initial powders with the molar ratio of Nb : Al : C = 4 : 1.1 : 2.7 [4].

3.2 Microstructure

The etched surface of Nb$_4$AlC$_3$ was shown in Fig. 4. Plate-like Nb$_4$AlC$_3$ grains distributed irregularly with a few equiaxed grains. The average grain size of Nb$_4$AlC$_3$ was 50 μm in length and 17 μm in width.
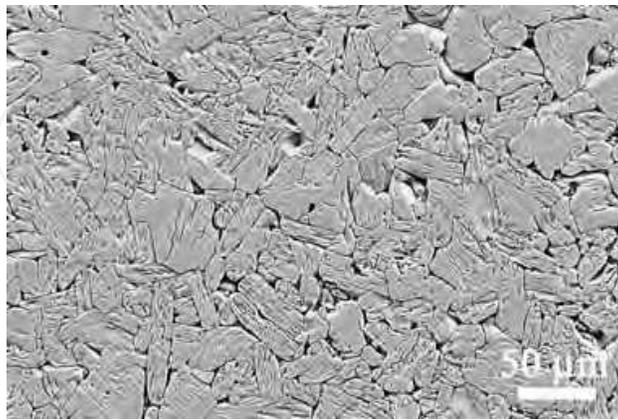
Fig. 4. Scanning electron microscope (SEM) micrograph of etched surface of Nb$_4$AlC$_3$ [4].

3.3 Properties evaluation
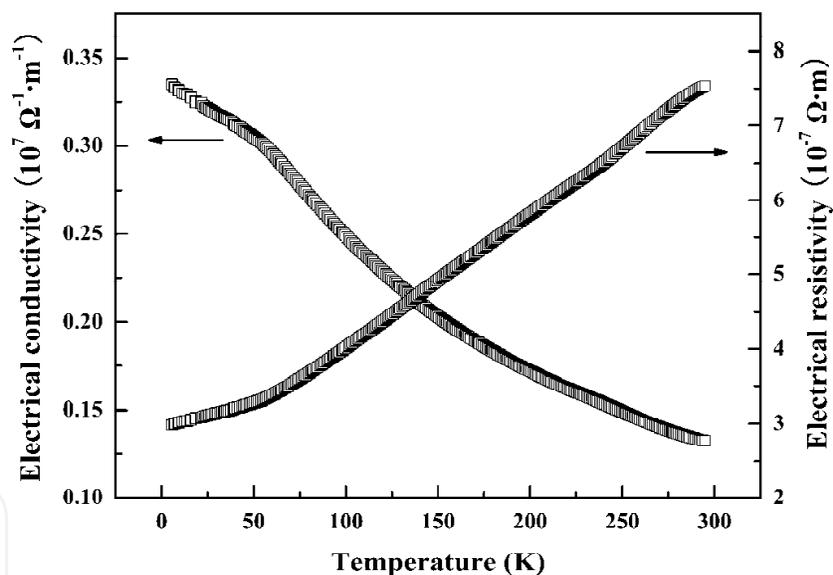
Fig. 5. Temperature dependences of electrical conductivity and electrical resistivity of Nb$_4$AlC$_3$ [4].

Figure 5 shows the electrical conductivity and electrical resistivity of Nb$_4$AlC$_3$ in the temperature range of 5-300 K. With the increasing temperature, the electrical conductivity of Nb$_4$AlC$_3$ decreased from 3.35×10^6 Ω^{-1}·m^{-1} to 1.33×10^6 Ω^{-1}·m^{-1}. The electrical resistivity of Nb$_4$AlC$_3$ increased linearly above 50 K, indicating a metallic characteristic. Fitting the resistivity in the temperature range from 50 to 300 K, the temperature dependence of electrical resistivity was obtained with a coefficient of determination, r^2, of 0.99:

$$\rho(\mu\Omega \cdot m) = \rho_0(1 - \beta\Delta T) = 7.133[1 - 0.0025(273.15 - T)] \tag{5}$$

where ρ_0 was the electrical resistivity at 273.15 K (μΩ·m), T the absolute temperature (K), and β the temperature coefficient of resistivity (K^{-1}). The temperature coefficient of resistivity was 0.0025 K^{-1}.

The thermal expansion coefficient of Nb$_4$AlC$_3$ was measured as 7.2 × 10^{-6} K^{-1} in the temperature range of 200-1100°C. Figure 6 shows the temperature dependences of molar heat capacity and thermal conductivity of Nb$_4$AlC$_3$. The molar heat capacity increased linearly with increment of temperature, which fitted a third-order polynomial. The molar heat capacity of Nb$_4$AlC$_3$ approached to a plateau above 1227°C. At room temperature, the molar heat capacity of Nb$_4$AlC$_3$ was determined as 158 J·(mol·K)$^{-1}$. A least square fitting the temperature dependence of thermal conductivity for Nb$_4$AlC$_3$ was described as:

$$\lambda = 11.6 + 0.0064T \qquad (6)$$

with r^2 of 0.99. At 25°C, the thermal conductivity of Nb$_4$AlC$_3$ was deduced to 13.5 W·(m·K)$^{-1}$. Up to 1227°C, the thermal conductivity of Nb$_4$AlC$_3$ increased to 21.2 W·(m·K)$^{-1}$. The total thermal conductivity was associated with both the electron and phonon contributions:

$$\lambda_{total} = \lambda_{electron} + \lambda_{phonon} \qquad (7)$$

in which $\lambda_{electron} = L_0 \sigma T$ (Wiedmann-Franz Law), where σ was the electrical conductivity at the selected temperature T, and $L_0 = 2.45 \times 10^{-8} W \cdot \Omega \cdot K^{-2}$. At room temperature, the calculated result was 9.6 W·(m·K)$^{-1}$, about 71% of total thermal conductivity. Therefore, the electrons mainly contributed to the conductivity at 25°C.
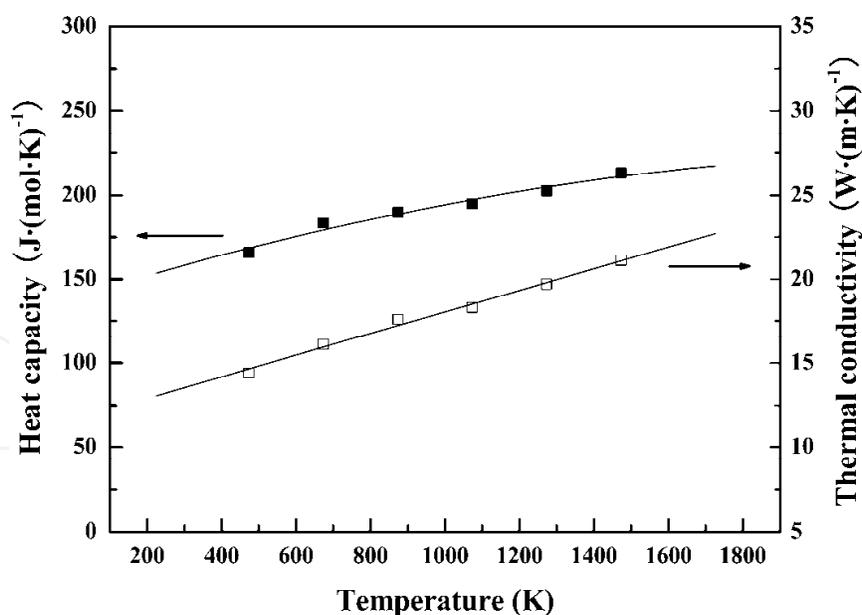

Fig. 6. Temperature dependences of molar heat capacity and thermal conductivity of Nb$_4$AlC$_3$ [4].

Figure 7 shows the indentation load dependence of Vickers hardness of Nb$_4$AlC$_3$. The insets were the Vickers indentation on the polished surface of Nb$_4$AlC$_3$ under a load of 10 N. With increasing load from 3 to 200 N, the hardness gradually decreased from 6.2 to 2.6 GPa. At a

lower load, the bigger scatter was seen due to the anisotropic nature of grains. Above 50 N, the hardness value converged to 2.6 GPa. Therefore, the intrinsic hardness of Nb$_4$AlC$_3$ was 2.6 GPa. The morphology of the indent produced by a load of 10 N showed that no cracks initiated and propagated from the diagonals, and the material was pushed out around the indent (Fig. 7(a)). The microscale plasticity was associated with infragrain multiple basal-plane slips between microlamellae, intergrain sliding, lamellae or grain push out, and microfailures at the ends of the constrained shear-slips (Fig. 7(b)). In addition, the zigzag crack propagation was observed in an individual Nb$_4$AlC$_3$ grain (Fig. 7(c)). Additionally, the measured shear strength of Nb$_4$AlC$_3$ was 116 MPa. The low shear strength implied good damage tolerance and easy machinability of Nb$_4$AlC$_3$.
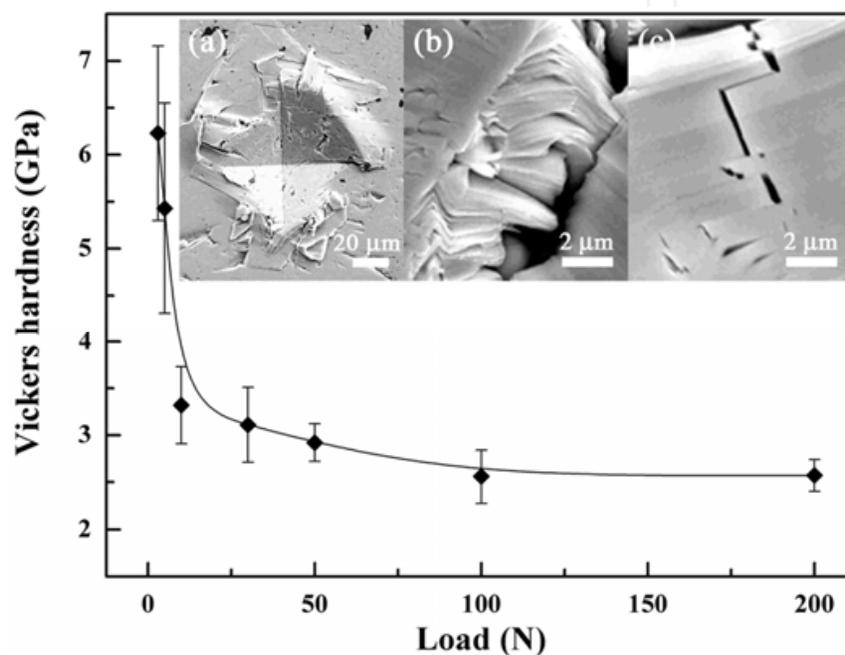
Fig. 7. Vickers hardness of Nb$_4$AlC$_3$ as a function of indentation loads. The insets show (a) push-out, (b) delamination, kink, and basal plane slips, and (c) zigzag crack propagation in a grain in an indent under a load of 10 N [4].

Figure 8(a) shows the temperature dependences of normalized Young's moduli of Nb$_4$AlC$_3$, Nb$_2$AlC, β-Ta$_4$AlC$_3$, and Ta$_2$AlC. The temperature dependences of mechanical damping, Q^{-1}, of Nb$_4$AlC$_3$, Nb$_2$AlC, β-Ta$_4$AlC$_3$, and Ta$_2$AlC were shown in Fig. 8(b). Below 1400°C, a slight linear decrease of Young's modulus of Nb$_4$AlC$_3$ was observed with increasing temperature. Whereas, a break was seen at a temperature between 1400 and 1500°C. Similar turning points were also observed at 1200-1300°C for Nb$_2$AlC, 800-900°C for β-Ta$_4$AlC$_3$, and 800-900°C for Ta$_2$AlC (Fig. 8(a)). Corresponding to the accelerated decrease of Young's modulus, the mechanical damping of Nb$_4$AlC$_3$ also started to increase at 1400°C (Fig. 8(b)). Above 1500°C, more rapid decrease of Young's modulus of Nb$_4$AlC$_3$ was observed with increasing temperature. The rapid decrease of Young's modulus started at 1300°C, 900°C, and 900°C, respectively, for Nb$_2$AlC, β-Ta$_4$AlC$_3$, and Ta$_2$AlC. The higher critical temperature for the rapid decrease of Young's modulus of Nb$_4$AlC$_3$ indicated that this material could be used at much higher temperatures. The Young's modulus of Nb$_4$AlC$_3$ could retain up to 1580°C with a loss of 21%. The modulus loss of Nb$_4$AlC$_3$ was 16% at 1400°C and 21% at 1580°C (Fig.

8(a)). Therefore, the flexural strength of Nb_4AlC_3 might still possess a high value up to 1580°C. Figure 9 displays the temperature dependence of flexural strength for Nb_4AlC_3. Obviously, the flexural strength of Nb_4AlC_3 could retain up to 1400°C without any degradation.
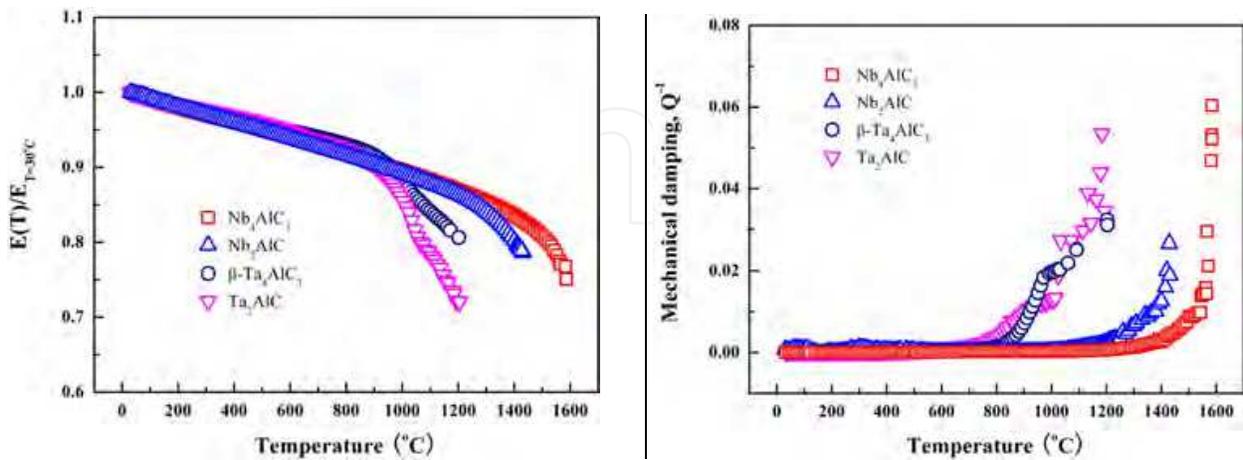

Fig. 8. Temperature dependences of (a) normalized Young's moduli and (b) mechanical damping, Q^{-1}, of Nb_4AlC_3, Nb_2AlC, β-Ta_4AlC_3, and Ta_2AlC [4].
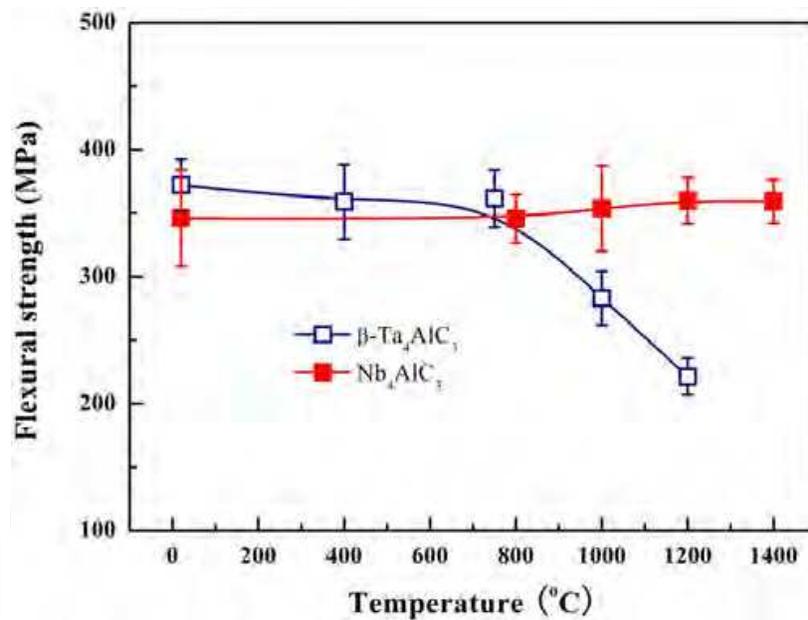

Fig. 9. Temperature dependent flexural strength of Nb_4AlC_3 and β-Ta_4AlC_3 [4].

4. Spark plasma sintering

4.1 Synthesis procedure

Commercial powders of niobium (45 μm, 99.9%), aluminum (30 μm, 99.9%), and carbon black (20 nm, 99%) were used for investigating the synthesis of Nb_4AlC_3 using the SPS technique. For investigating the reaction path, niobium, aluminum, and carbon black powders with a molar ratio of 4 : 1.5 : 2.7 were weighed using an electrical balance with an accuracy of 10^{-2} g. The powders were put into an agate jar and milled for 12 hours using

ethanol as the dispersant. After milling, the mixed powders were dried in air and sieved using a 100 mesh sieve. The obtained mixture was put into a graphite die with a diameter of 20 mm. A layer of carbon sheet (~0.2 mm thickness) was put in the inner of die for lubrication. A layer of heat isolation carbon fiber was used to wrap the die for inhibiting the rapid heat diffusion. The mixture was firstly cold pressed as a compact green. Then the green together with the die was heated in a spark plasma sintering facility (100 kN SPS-1050, Syntex Inc., Japan). The sintering temperature was measured by an optical pyrometer focusing on a hole in the wall of die. From ambient temperature to 700°C, it took 5 minutes to heat the sample. Between 700 and 1400°C, a heating speed of 50°C/min was adopted. Above 1400°C, the heating speed was set as 10°C/min. The annealing temperatures were selected as 800, 1000, 1200, 1400, and 1600°C, respectively. The vacuum degree was 7-10 Pa. The holding time was 2 minutes.
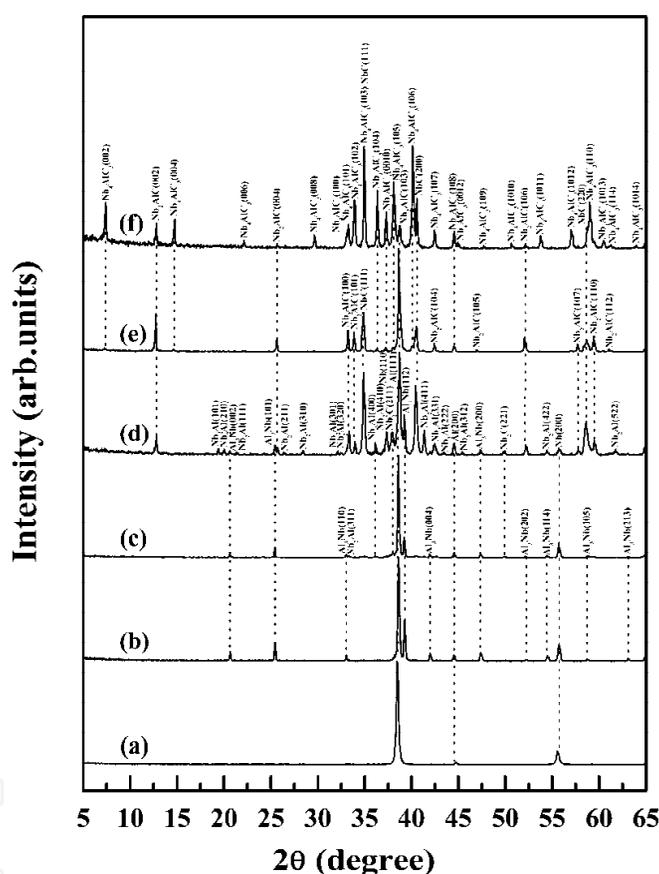

Fig. 10. XRD patterns of samples sintered at different temperatures using Nb, Al, and carbon black mixture powders with the molar ratio of 4 : 1.5 : 2.7: (a) ambient temperature, (b) 800°C, (c) 1000°C, (d) 1200°C, (e) 1400°C, and (f) 1600°C [5].

Figure 10 shows XRD patterns of samples sintered from ambient temperature to 1600°C using Nb, Al, and carbon black mixture powders with the molar ratio of 4 : 1.5 : 2.7. The XRD data of initial mixture powder was shown in Fig. 10(a). Carbon black could not be detected, which might be due to the fine structure. When the temperature was increased to 800°C, Al$_3$Nb was detected in the sample by XRD (Fig. 10(b)). The melting point of aluminum was 660°C, which meant that the melting aluminum probably combined niobium to form Al$_3$Nb during the heating process:

$$3Al(l) + Nb(s) \rightarrow Al_3Nb(s) \tag{8}$$

When increasing the temperature up to 1000°C, Nb$_2$Al and Nb$_2$C appeared in the sample with the consumption of Al$_3$Nb (Fig. 10(c)). The reaction could be possibly described as:

$$Al_3Nb(s) + 5Nb(s) \rightarrow 3Nb_2Al(s) \tag{9}$$
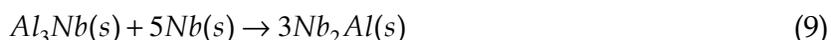
Additionally, Nb$_2$C was formed due to the reaction between Nb and carbon black:

$$2Nb(s) + C(s) \rightarrow Nb_2C(s) \tag{10}$$

As temperature increased to 1200°C, the diffraction analysis showed that new phases of NbC and Nb$_2$AlC became the main phases in the sintered sample (Fig. 10(d)). The amounts of Nb$_2$Al and Nb$_2$C also increased with the consumption of Nb, Al, and Al$_3$Nb. Probably, the formation of NbC was ascribed to the reaction:

$$Nb(s) + C(s) \rightarrow NbC(s) \tag{11}$$

Nb$_2$AlC was probably formed due to the reaction between Nb$_2$Al and carbon black. The reaction equation was described as:

$$Nb_2Al(s) + C(s) \rightarrow Nb_2AlC(s) \tag{12}$$

When the temperature increased up to 1400-1600°C, the existed phases in the samples were only NbC, Nb$_2$AlC, and Nb$_4$AlC$_3$. In hot pressing, it was found that Nb$_3$Al$_2$C existed in the sample sintered by hot pressing at 1500°C. Due to the initial composition difference (Nb : Al : C = 4 : 1.3 : 2.7), it might be due to the kinetics of phase formation. At 1400°C, Nb$_4$AlC$_3$ was detected in the prepared sample (Fig. 10(e)). Probably, it was ascribed to the following two equations:

$$Nb_2AlC(s) + Nb_2C(s) + C(s) \rightarrow Nb_4AlC_3(s) \tag{13}$$

and

$$Nb_2AlC(s) + 2NbC(s) \rightarrow Nb_4AlC_3(s) \tag{14}$$
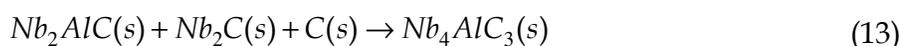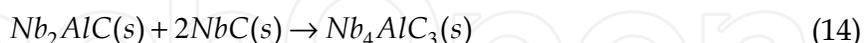
It was supposed that carbon black has been completely consumed at this temperature. When the temperature rose to 1600°C, Nb$_4$AlC$_3$ became the main phase with the consumption of Nb$_2$AlC and NbC (Fig. 10(f)).

In order to get single phase Nb$_4$AlC$_3$, the sintering temperature was further increased. Figure 11 shows the effect of annealing temperatures on the synthesis of Nb$_4$AlC$_3$. When the annealing temperature was 1620°C, only Nb$_4$AlC$_3$ and Nb$_2$AlC could be detected in the sample (Fig. 11(a)). NbC has been completely consumed during the reaction process (Eq. (14)). When increasing the temperature as 1650°C, less Nb$_2$AlC could be detected in the sample by XRD (Fig. 11(b)). However, Al$_3$Nb appeared again:

$$9Nb_2AlC(s) \rightarrow 3Nb_4AlC_3(s) + 2Al_3Nb(s) + 4Nb(s) \tag{15}$$
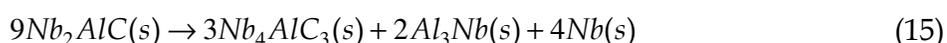
When the annealing temperature was increased up to 1665°C, more Al_3Nb was formed and a small quantity of NbC also appeared in the sample (Fig. 11(c)). NbC was from the decomposition of Nb_4AlC_3 due to the loss of Al. Up to 1680°C, the amount of NbC increased and Al_3Nb disappeared in the sample (Fig. 11(d)). The optimized annealing temperature in present work was 1650°C.
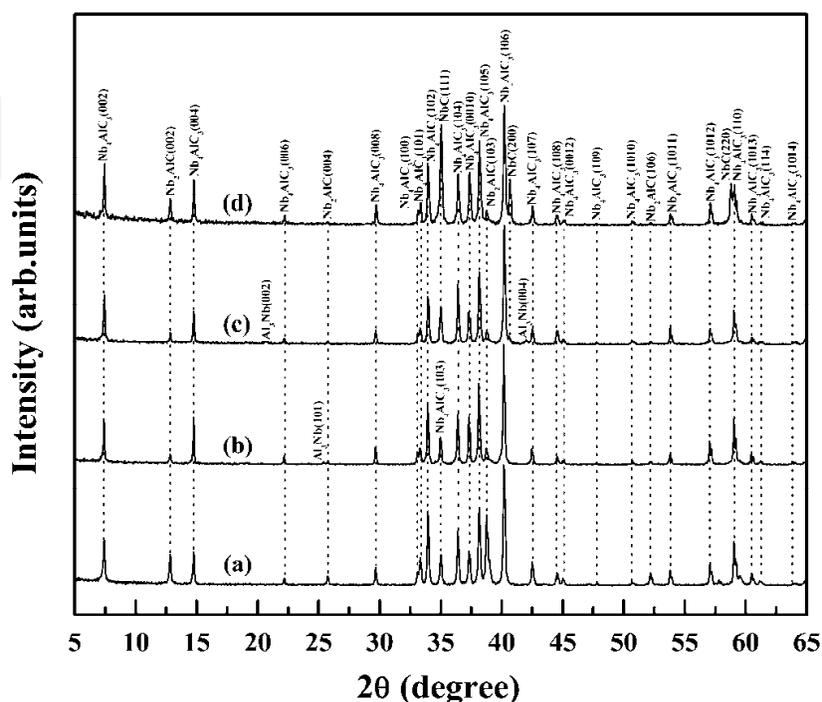

Fig. 11. Effect of annealing temperature on the synthesis of Nb_4AlC_3: (a) 1620°C, (b) 1650°C, (c) 1665°C, and (d) 1680°C [5].

In order to investigate the effect of initial composition on the synthesis of Nb_4AlC_3, the initial mixture powders with different molar ratios of Nb : Al : C = 4 : 1.1 : 2.7, 4 : 1.3 : 2.7, 4 : 1.4 : 2.7, and 4 : 1.5 : 2.7 were selected and sintered at the optimized temperature of 1650°C. Figure 12 shows the XRD patterns of sintered samples. With the increasing Al content in the initial compositions, the amount of NbC in the sample decreased continuously (Figs. 12(a)-(d)). The optimized composition for synthesizing Nb_4AlC_3 by hot pressing in a flowing argon atmosphere was Nb : Al : C = 4 : 1.1 : 2.7. Because of the high vacuum level in SPS furnace (7-10 Pa), Al element was easier to evaporate at high temperature. Therefore, more Al element was added into the compositions. When the initial composition of Nb : Al : C = 4 : 1.5 : 2.7 was used for preparing Nb_4AlC_3, there were only a small quantity of Nb_2AlC and a trace of Al_3Nb existing in the sample. Therefore, the optimized composition was selected as 4 : 1.5 : 2.7. Additionally, it was hoped to eliminate the impurities of Nb_2AlC and Al_3Nb by modifying the holding time. However, when prolonging the holding time from 2 to 4 minutes, though Al_3Nb has disappeared, a plenty of NbC appeared in the sample and Nb_2AlC couldn't be removed, as shown in Fig. 13. Therefore, the optimized holding time in present work was 2 minutes.

Based on the above investigations, the optimized parameters were used to synthesize dense bulk Nb_4AlC_3. Figure 14 shows the X-ray diffraction pattern of as-prepared Nb_4AlC_3. The

primary phase was Nb_4AlC_3 and a few amount of Nb_2AlC and Al_3Nb existed in the sample. The impurities of Nb_2AlC and Al_3Nb were less than 6 wt%.
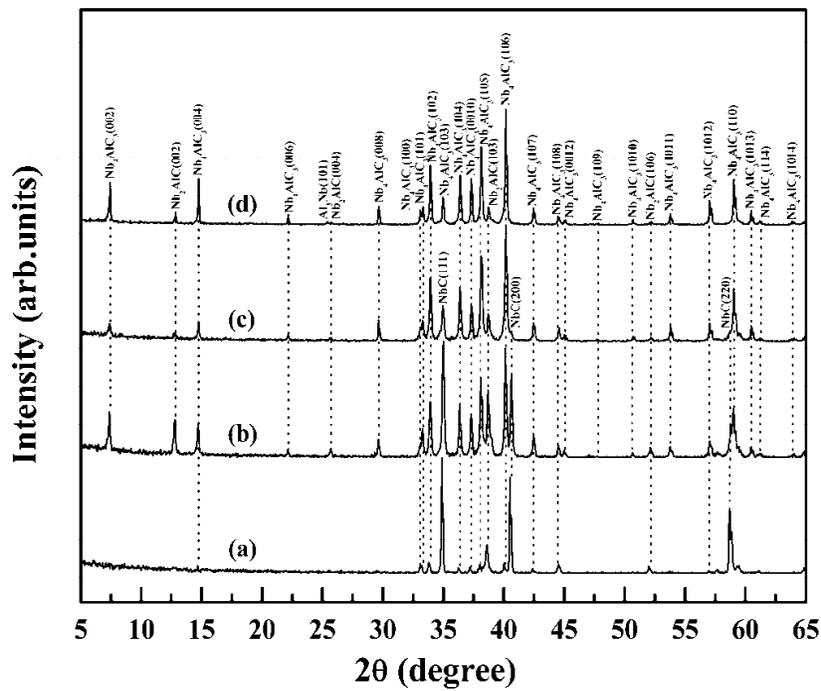

Fig. 12. Effect of initial element compositions (molar ratio of Nb, Al, and C) on the synthesis of Nb_4AlC_3: (a) 4 : 1.1 : 2.7, (b) 4 : 1.3 : 2.7, (c) 4 : 1.4 : 2.7, and (d) 4 : 1.5 : 2.7 [5].
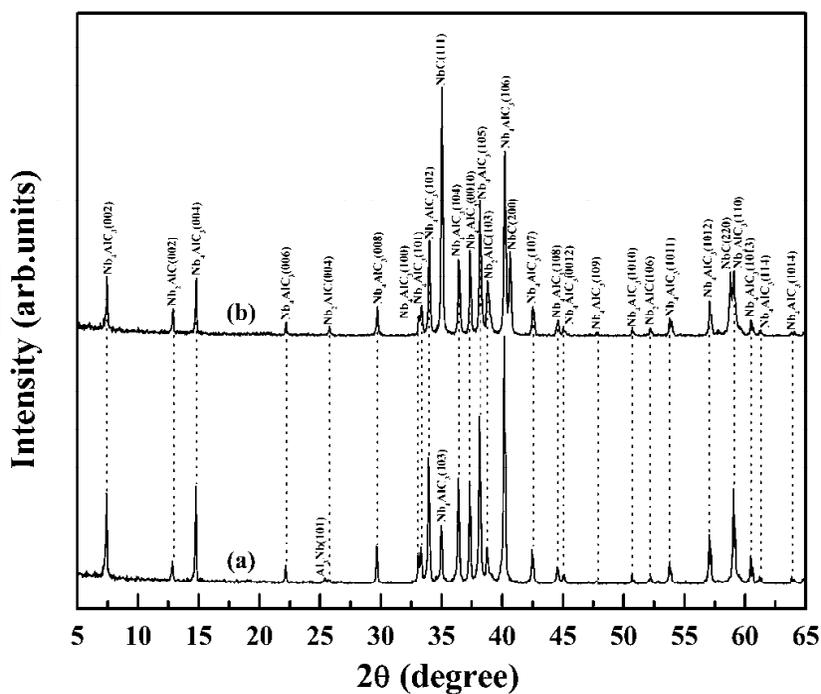

Fig. 13. Effect of holding time on the synthesis of Nb_4AlC_3: (a) 2 minutes and (b) 4 minutes [5].
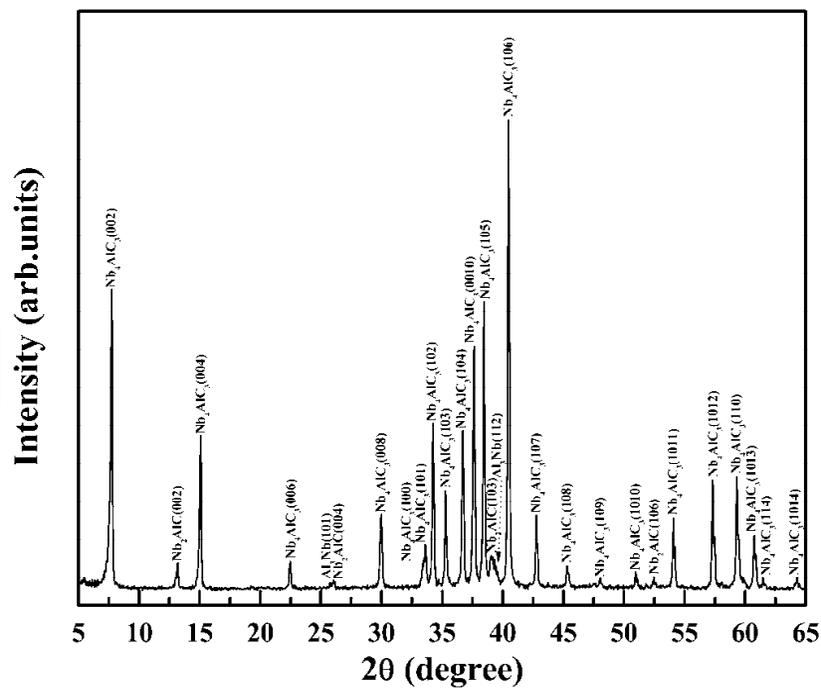
Fig. 14. XRD pattern of dense Nb$_4$AlC$_3$ synthesized using the optimized parameters under a pressure of 30 MPa [5].

4.2 Microstructure

Figure 15 shows the etched surface and fracture surface of Nb$_4$AlC$_3$. Laminar grains could be clearly observed in the etched surface. The growth of grain did not show the preferable direction, i.e., textured microstructure. The mean grain size was determined as 21 μm in length and 9 μm in width. In the fracture surface, Nb$_4$AlC$_3$ grains exhibited the multiplex damage modes, such as transgranular fracture, intergranular fracture, kink bands, and delaminations.
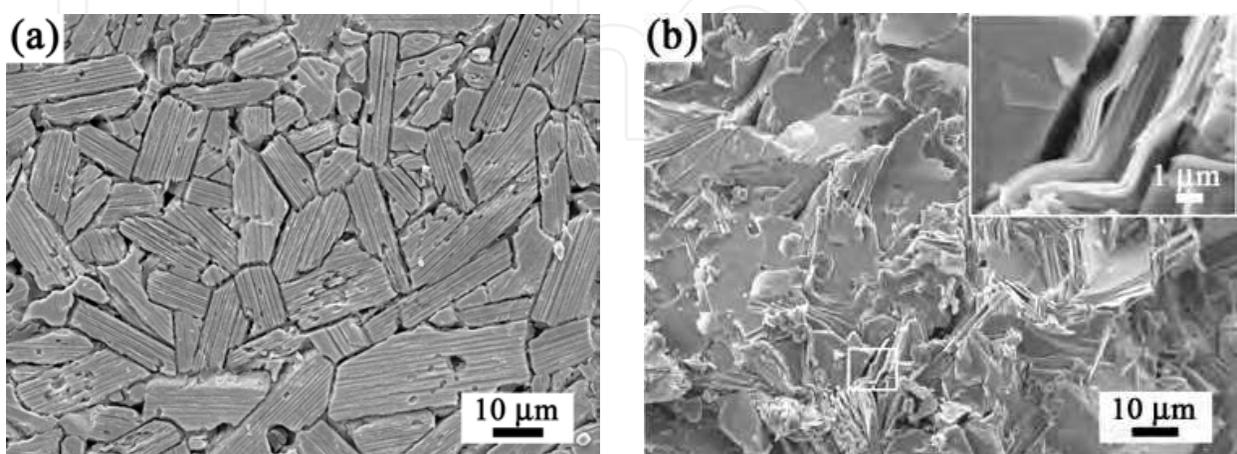
Fig. 15. SEM micrographs of (a) etched surface and (b) fracture surface of dense Nb$_4$AlC$_3$ sample [5].

4.3 Properties evaluation

The thermal expansion and technical thermal expansion coefficient of Nb_4AlC_3 sample were shown in Fig. 16. With increasing temperature, the thermal expansion of Nb_4AlC_3 showed the linear change. Fitting the thermal expansion in the temperature range from -128 to 282°C, the temperature dependence of thermal expansion was obtained with a coefficient of determination, r^2, of 0.99:

$$\frac{\Delta L}{L_0} = -0.18204 + 6.5483 \times 10^{-4} T \tag{16}$$

in which ΔL (m) was the length change at temperature T (K), and L_0 (m) was the length of sample at 5°C (initial room temperature). The technical thermal expansion coefficient, $\alpha_{tech.}$ (K^{-1}), was defined as:

$$\alpha_{tech.} = \frac{1}{L_{145K}} \frac{\Delta L_K - \Delta L_{145K}}{T_K - 145} \tag{17}$$

in which L_{145K} (m) was the length of sample at -128°C, ΔL_{145K} (m) the length change at -128°C, and ΔL_K (m) the length change at temperature T_K (K). The calculated thermal expansion coefficient at 282°C was 6.7×10^{-6} K^{-1}. The technical thermal expansion coefficient of Nb_4AlC_3 increased from -128 to about -73°C rapidly, which might be attributed to the nonlinear increase of instrument temperature. Above -73°C, the technical thermal expansion coefficient approached a constant.
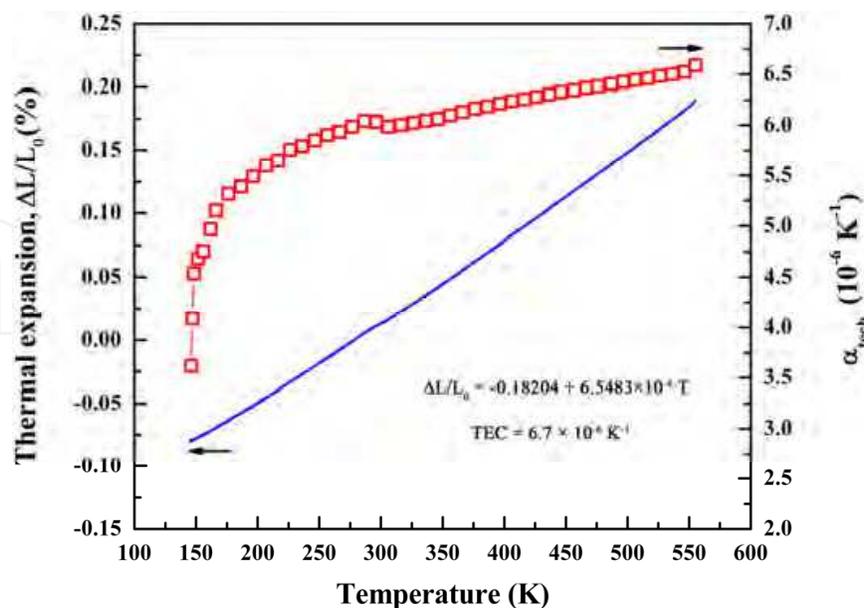

Fig. 16. Temperature dependence of thermal expansion and technical thermal expansion coefficient of Nb_4AlC_3 in a temperature range of -128 and 282°C [5].

Figure 17 shows the temperature dependent electrical conductivity and electrical resistivity of Nb$_4$AlC$_3$ in a temperature range of 25-827°C. With increasing temperature, the electrical conductivity decreased corresponding to the increase of electrical resistivity. The measured electrical conductivity of Nb$_4$AlC$_3$ at 25°C was 2.25 × 10^6 Ω^{-1} m^{-1}, higher than that of hot pressed sample (1.33 × 10^6 Ω^{-1} m^{-1}), which might be due to the existence of Nb$_2$AlC (3.45 × 10^6 Ω^{-1} m^{-1}) and Al$_3$Nb. The electrical resistivity of Nb$_4$AlC$_3$ increased with a linear rule below 300°C. Fitting the electrical resistivity in the temperature range of 25-300°C, the temperature dependent resistivity could be obtained with a determination coefficient of 0.99:

$$\rho(\mu\Omega \cdot m) = \rho_0(1 - \beta\Delta T) = 0.44371[1 - 0.003048(298 - T)] \tag{18}$$

in which ρ_0 was the electrical resistivity at 298 K (μΩ·m), T the absolute temperature (K), and β the temperature coefficient of resistivity (K^{-1}). However, the temperature dependent electrical resistivity showed the nonlinear increase above 300°C with the increment of temperature. At 827°C, Nb$_4$AlC$_3$ still had a high electrical conductivity of 0.76 × 10^6 Ω^{-1} m^{-1}, indicating the excellent high temperature conductive capability.
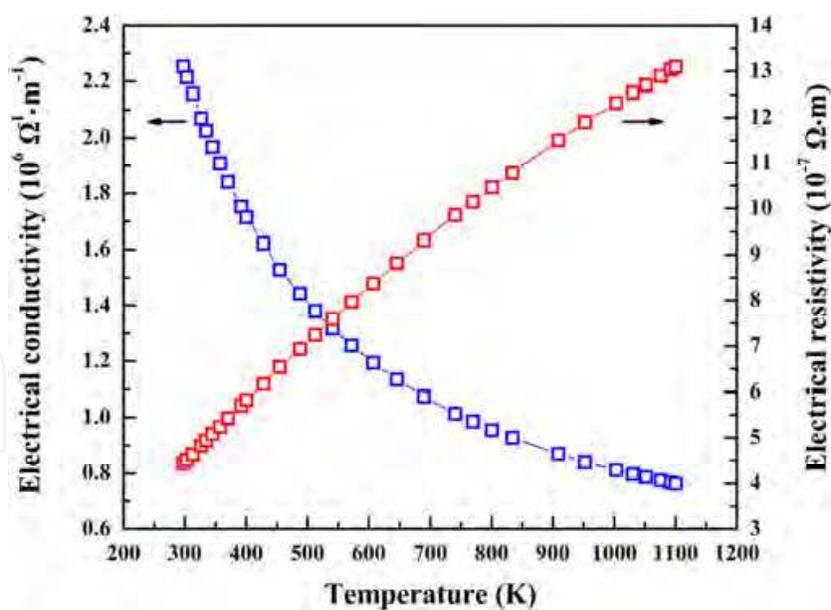

Fig. 17. Temperature dependence of electrical conductivity of Nb$_4$AlC$_3$ in a temperature range of ambient temperature and 827°C [5].

The measured Vickers hardness of as-prepared Nb_4AlC_3 was 3.7 GPa, which was close to the value of hot pressed Nb_4AlC_3. Figure 18 displays the three cycles load versus depth-of-microindentation of one Nb_4AlC_3 grain whose basal plane was perpendicular to the surface. Inset was the loops of single cycle indentation on both perpendicular (PE) and parallel (PA) directions, in comparison with that of ZrB_2. The three indentation cycles were all open without reversibility. However, the open scope, i.e., loop area, was decreasing with more cycles, which showed the slight harder behavior. Additionally, the indentation responses were different along PA and PE directions. Obviously, the indentation depth and loop area along PA direction were larger than those along PE direction. It was easier to form kink bands along PA direction because the top surface was unconstrained. Pop-in appeared during the indentation when along PE direction, which was probably due to the delaminations between basal planes. In comparison with the hexagonal ZrB_2, the smaller elastic recovery indicated the more effective energy dispersive capability.
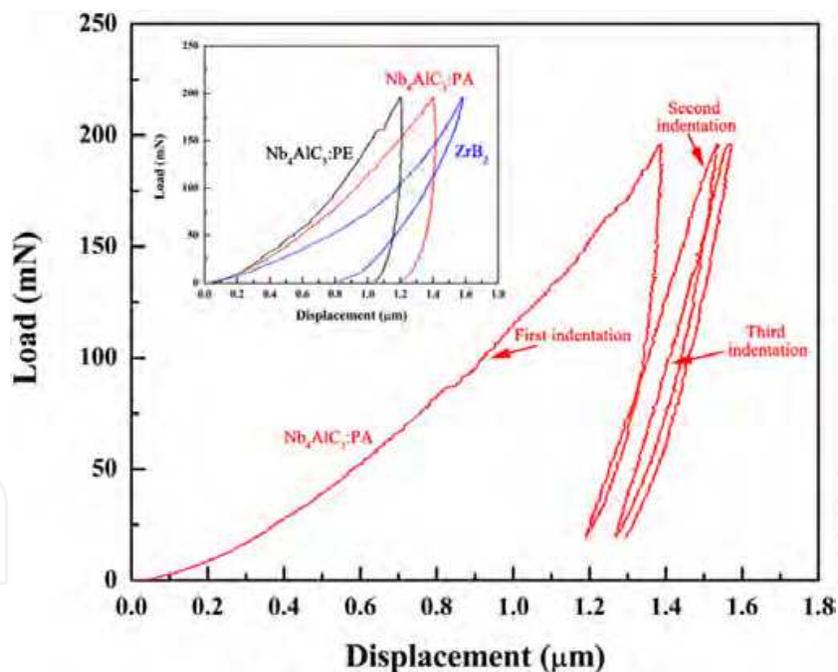

Fig. 18. Typical load vs. depth of indentation response of one Nb_4AlC_3 grain whose basal plane is perpendicular to the surface. Inset is the loops of single indentation on both perpendicular (PE) and parallel (PA) directions, in comparison with that of ZrB_2 (hexagonal structure) [5].

The ambient flexural strength of Nb$_4$AlC$_3$ was tested as 455 MPa, higher than that of hot pressed Nb$_4$AlC$_3$ (346 MPa), which might be ascribed to the finer grain size. When the samples were tested at 1000 and 1400°C, the flexural strength of Nb$_4$AlC$_3$ were 297 and 230 MPa, respectively. The decrease of flexural strength might be ascribed to the existence of Al$_3$Nb in the samples, which caused the plasticity deformation of bars at high temperatures.

5. Summary

In this chapter, bulk Nb$_4$AlC$_3$ ceramic was prepared by an *in situ* reaction/hot pressing method and spark plasma sintering using Nb, Al, and carbon as the starting materials. The reaction path was investigated. Additionally, it was found that when different sintering methods were adopted the final properties of ceramic were different. *Hot pressing*: The thermal expansion coefficient was determined as 7.2×10^{-6} K^{-1} in the temperature range of 200-1100°C. The thermal conductivity of Nb$_4$AlC$_3$ increased from 13.5 W$\cdot$(m$\cdot$K)$^{-1}$ at room temperature to 21.2 W$\cdot$(m$\cdot$K)$^{-1}$ at 1227°C, and the electrical conductivity decreased from 3.35×10^6 to 1.13×10^6 $\Omega^{-1}\cdot$m^{-1} in a temperature range of 5-300 K. Nb$_4$AlC$_3$ possessed a low hardness of 2.6 GPa and high flexural strength of 346 MPa. Most significantly, Nb$_4$AlC$_3$ could retain high modulus and strength up to very high temperatures. The Young's modulus at 1580°C was 241 GPa (79% of that at room temperature), and the flexural strength could retain the ambient strength value without any degradation up to the maximum measured temperature of 1400°C. *Spark plasma sintering*: The coefficient of thermal expansion was measured as 6.7×10^{-6} K^{-1} from -128 to 282°C. The electrical conductivity was tested as 0.76×10^6 $\Omega^{-1}\cdot$m^{-1} at 827°C, showing excellent high temperature conductivity. The Vickers hardness and flexural strength were measured as 3.7 GPa and 455 MPa, respectively. The micro-indentation evaluation indicated the anisotropic response of Nb$_4$AlC$_3$ grains, reflecting the anisotropic crystal structure. Additionally, the flexural strength could remain a high value of 230 MPa up to 1400°C.

6. References

[1] H. Nowotny, "Struktuchemie Einiger Verbindungen Der Ubergangsmetalle Mit Den Elementen C, Si, Ge, Sn," *Prog. Solid State Chem.*, 2, 27 (1970).

[2] M. W. Barsoum, "The M$_{N+1}$AX$_N$ Phases: A New Class of Solids; Thermodynamically Stable Nanolaminates," *Prog. Solid State Chem.*, 28, 201-81 (2000).

[3] C. F. Hu, F. Z. Li, J. Zhang, J. M. Wang, J. Y. Wang, and Y. C. Zhou, "Nb$_4$AlC$_3$: A New Compound Belonging to the MAX Phases," *Scripta Mater.*, 57, 893-6 (2007).

[4] C. F. Hu, F. Z. Li, L. F. He, M. Y. Liu, J. Zhang, J. M. Wang, Y. W. Bao, J. Y. Wang, and Y. C. Zhou, "*In Situ* Reaction Synthesis, Electrical and Thermal, and Mechanical Properties of Nb$_4$AlC$_3$," *J. Am. Ceram. Soc.*, 91, 2258-63 (2008).

[5] C. F. Hu, Y. Sakka, H. Tanaka, T. Nishimura, and S. Grasso, "Low Temperature Thermal Expansion, High Temperature Electrical Conductivity, and Mechanical Properties of Nb_4AlC_3 Ceramic Synthesized by Spark Plasma Sintering," *J. Alloys Compd.*, 487, 675-81 (2009).
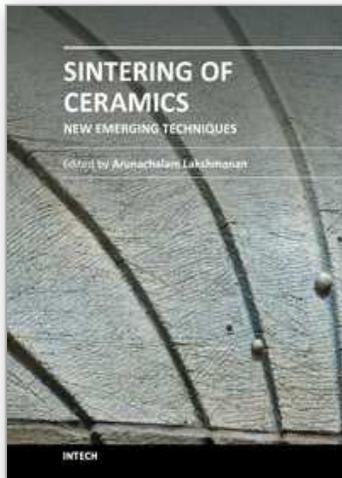
Sintering of Ceramics - New Emerging Techniques

Edited by Dr. Arunachalam Lakshmanan

The chapters covered in this book include emerging new techniques on sintering. Major experts in this field contributed to this book and presented their research. Topics covered in this publication include Spark plasma sintering, Magnetic Pulsed compaction, Low Temperature Co-fired Ceramic technology for the preparation of 3-dimesinal circuits, Microwave sintering of thermistor ceramics, Synthesis of Bio-compatible ceramics, Sintering of Rare Earth Doped Bismuth Titanate Ceramics prepared by Soft Combustion, nanostructured ceramics, alternative solid-state reaction routes yielding densified bulk ceramics and nanopowders, Sintering of intermetallic superconductors such as MgB2, impurity doping in luminescence phosphors synthesized using soft techniques, etc. Other advanced sintering techniques such as radiation thermal sintering for the manufacture of thin film solid oxide fuel cells are also described.

How to reference

In order to correctly reference this scholarly work, feel free to copy and paste the following:

INTECH
open science | open minds